Nucleic Acids Research, 2025, **53**, gkaf508
https://doi.org/10.1093/nar/gkaf508
Chemical Biology and Nucleic Acid Chemistry

Impact of a single 8-oxoguanine lesion on Watson–Crick and Hoogsteen base pair hybridization in telomeric DNA quantified using single-molecule force spectroscopy

Yuanlei Cheng[1,2,*,†], **Ximin Wang**[2,†], **Xuyang Yang**[2], **Yashuo Zhang**[2], **Huijuan You**[2,*]

[1]Department of Pharmacy, The Central Hospital of Wuhan, Tongji Medical College, Huazhong University of Science and Technology, Wuhan 430014, China
[2]Hubei Key Laboratory of Natural Medicinal Chemistry and Resource Evaluation, School of Pharmacy, Tongji Medical College, Huazhong University of Science and Technology, Wuhan 430030, China

[*]To whom correspondence should be addressed. Email: youhuijuan@hust.edu.cn
Correspondence may also be addressed to Yuanlei Cheng. Email: Cheng302024@163.com
[†]The first two authors should be regarded as Joint First Authors.

Abstract

8-Oxoguanine ($^{8\text{-oxo}}$G) is a common DNA oxidative lesion prevalent in telomeric regions. However, the impact of $^{8\text{-oxo}}$G modification on the Watson–Crick base pairing energy remains controversial, potentially due to the formation of partially folded intermediates. Here, we used single-molecule magnetic tweezers to characterize the mechanical stability and equilibrium folding/unfolding transitions of human telomeric hairpins containing a single $^{8\text{-oxo}}$G lesion at different positions. Our results reveal that fully folded hairpins with a centrally located $^{8\text{-oxo}}$G exhibit similar hybridization energy ($\Delta\Delta G \sim 1\ k_B T$) and folding/unfolding rates to the wild type. This provides valuable data for refining the energy contribution of $^{8\text{-oxo}}$G-C base pair. In contrast, a single $^{8\text{-oxo}}$G lesion near the unzipping termini (5′-end or 3′-end) significantly enhances end fraying and hinders the complete folding of the hairpin under force. A 5′-end $^{8\text{-oxo}}$G lesion increased the unfolding rates by a 130-fold compared to the wild type at 10.1 pN. These findings provide insights into the unzipping dynamics of DNA duplexes containing $^{8\text{-oxo}}$G lesions at replication and transcription forks. Furthermore, we observed that an $^{8\text{-oxo}}$G at 5′-end of telomeric G-quadruplexes (G4s) significantly decreases folding rates and folding free energy (from 5.9 $k_B T$ to 2.3 $k_B T$), shedding light on the dynamics of G4s under oxidative stress.

Graphical abstract

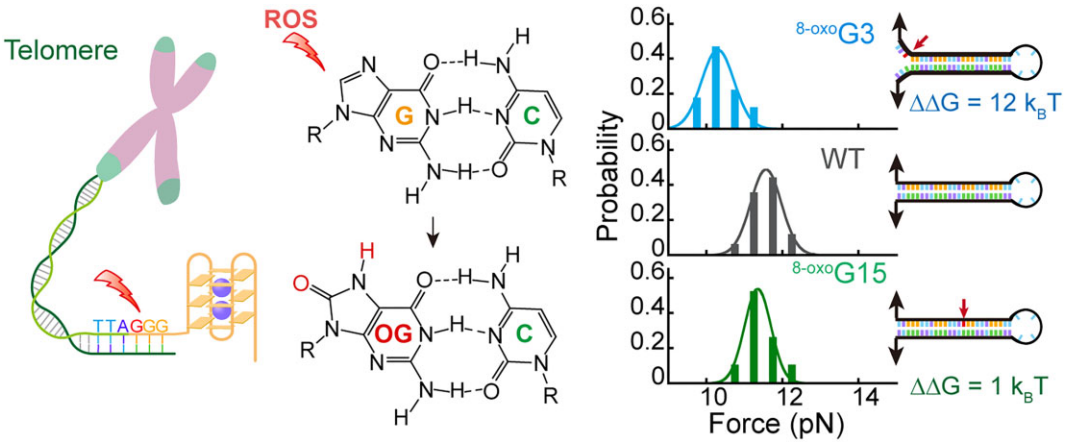

Introduction

Cellular DNA is constantly exposed to endogenous and exogenous reactive oxygen species, causing the formation of oxidative DNA lesions [1]. Among the four DNA nucleobases, guanine is particularly vulnerable to oxidation due to its low reduction potential [2], resulting in the formation of 8-oxo-7,8-dihydro-2′-deoxyguanosine ($^{8\text{-oxo}}$G), where a hydrogen atom is replaced by an oxygen atom at the C8 position and the N7 nitrogen becomes protonated. $^{8\text{-oxo}}$G is one of the most common oxidative lesions [3], as it has been estimated that each human cell experiences over 2800 $^{8\text{-oxo}}$G events per day [1]. The accumulation of $^{8\text{-oxo}}$G lesions can compromise

Received: January 8, 2025. **Revised:** May 11, 2025. **Editorial Decision:** May 26, 2025. **Accepted:** May 30, 2025
© The Author(s) 2025. Published by Oxford University Press on behalf of Nucleic Acids Research.
This is an Open Access article distributed under the terms of the Creative Commons Attribution-NonCommercial License (https://creativecommons.org/licenses/by-nc/4.0/), which permits non-commercial re-use, distribution, and reproduction in any medium, provided the original work is properly cited. For commercial re-use, please contact reprints@oup.com for reprints and translation rights for reprints. All other permissions can be obtained through our RightsLink service via the Permissions link on the article page on our site—for further information please contact journals.permissions@oup.com.

genomic integrity, potentially leading to mutagenesis and cell death [1].

Telomeres, the protective caps at the end of chromosomes, are particularly susceptible to oxidative damage. Human telomeres consist of tandem repeats of the 5′-TTAGGG sequence, with a 2–15-kb double-stranded DNA (dsDNA) and a single-stranded 3′ overhang of 50–300 nucleotides [4]. The high guanine content makes telomeric repeats especially vulnerable to oxidation, with contiguous G-tracts more susceptible than isolated guanine [5]. Oxidative damage can accelerate telomere shortening, a process associated with aging and cellular senescence [6]. Moreover, $^{8\text{-oxo}}$G can interfere with telomerase activity, the enzyme responsible for maintaining telomere length [6]. Besides the canonical duplex structures, the telomeric repeat sequences also can fold into four-stranded G-quadruplex structures, where four guanine bases are linked by Hoogsteen hydrogen bonds [5, 7–9]. Substitutions of guanine with $^{8\text{-oxo}}$G in telomeric DNA sequences have been shown to destabilize G-quadruplexes (G4s) and interfere with their functions [10–12].

Understanding the effects of $^{8\text{-oxo}}$G lesions on DNA stability and folding/unfolding dynamics is crucial for assessing their impact on various biological functions, including DNA replication fidelity [13]. $^{8\text{-oxo}}$G lesions can affect DNA duplex folding (hybridization) and unfolding (dehybridization) dynamics, thus leading to errors during DNA replication, potentially increasing the risk of mutations and impacting genome stability [14]. The nearest-neighbor (NN) model predicts the hybridization energy of the duplex by summing the energy contributions of adjacent NN base pair stacks, which has been extensively used in tools like Mfold [15], DINAMelt [16], and NUPACK [17] to predict melting temperatures. The NN model parameters are primarily derived from melting experiments [14], single-molecule force spectroscopy [18, 19], and molecular dynamics/quantum mechanics prediction [20]. However, the parameters for accurately predicting the hybridization energies for DNA duplexes containing $^{8\text{-oxo}}$G lesions remain lacking because controversial experimental results have been reported [21–23].

X-ray crystallography and nuclear magnetic resonance (NMR) studies have shown that the $^{8\text{-oxo}}$G-C (cytosine) base pair closely resembles the undamaged Watson–Crick G-C base pair, with minimal disruption to hydrogen bonds and stacking interactions [24, 25]. Although $^{8\text{-oxo}}$G can form a Watson–Crick base pair with cytosine similar to guanine (Fig. 1A), its impact on DNA duplex stability remains controversial. Previous studies have revealed that an $^{8\text{-oxo}}$G substitution can slightly destabilize duplexes [21, 22]. The melting temperature (T_m) analysis showed an ∼2°C reduction in T_m, corresponding to a 2.0 kcal/mol free energy difference measured using 10–15-bp duplexes in the presence of 1 M NaCl or KCl [21, 22]. DNA NMR imino proton exchange analysis also revealed that $^{8\text{-oxo}}$G-C did not inceraseed opening kinetics relative to G-C pair [26]. However, studies using shorter DNA duplexes revealed a more significant T_m reduction (∼13.8°C) in the presence of 100 mM NaCl [23]. Nevertheless, during the melting measurements, multiple partially folded species can coexist, thus causing difficulties in accurately quantifying the stability.

Single-molecule techniques, such as force spectroscopy [27] and nanopore technology [22], offer advantages over bulk methods for quantifying the thermodynamic parameters because the two-state assumption applied to melting curve analysis is not needed. Force-based unzipping experiments provide valuable insights into the mechanisms underlying DNA replication, where enzymes such as polymerases and helicases exert forces on dsDNA and open it up to form replication forks [28]. Unlike thermal melting, the directional unzipping by force mimics the directional movement of replication forks. These approaches enable accurate measurements of DNA thermodynamics and kinetics, including the effects of $^{8\text{-oxo}}$G substitutions [27], mismatches (e.g. G-A pairs) [29, 30], and methylation (5-methyl-cytosine) [31]. Previous single-molecule stretching experiments on a 29-bp DNA hairpin with two $^{8\text{-oxo}}$G substitutions showed an ∼20.8 k_BT reduction in hybridization-free energy as each $^{8\text{-oxo}}$G-C site reduces ∼6.4 k_BT [27]. However, the observed reduced step sizes (55.8–38.7 nt) suggested that the first seven to eight bases of the hairpin stem remained open, implying the formation of partially folded structures. Therefore, the intrinsic stability of the $^{8\text{-oxo}}$G-C base pair remained uncertain.

Here, we employed single-molecule magnetic tweezers to investigate the impact of a single $^{8\text{-oxo}}$G lesion on the folding/unfolding dynamics of telomeric DNA duplex and G4s containing $^{8\text{-oxo}}$G. By strategically placing a single $^{8\text{-oxo}}$G near the 5′-end and in the middle of hairpin structures, we were able to differentiate the end-fraying effects and the impact of $^{8\text{-oxo}}$G-C base pair stability on overall hairpin stability. By analyzing the folding/unfolding dynamics at constant forces, we quantified the effects of $^{8\text{-oxo}}$G on the Watson–Crick base pair energy and folding/unfolding kinetics. While previous studies have explored the effects of $^{8\text{-oxo}}$G modifications on the mechanical stability and folding/unfolding dynamics of G4s using various single-molecule techniques, such as nanopore technology [32], fluorescence resonance energy transfer [33], and optical tweezers [34], the impact of $^{8\text{-oxo}}$G at the 5′-end of a 5′-GGG tract, a highly oxidizable site [3, 5, 35], remains largely unexplored. Therefore, we also quantified the impact of a single $^{8\text{-oxo}}$G modification at the 5′-end of G4s using single-molecule magnetic tweezers.

Materials and methods

DNA sample preparation

All oligonucleotides were purchased from Sangon Biotech (China) (Supplementary Table S1). To prepare the 5′-thiol-labeled 489-bp and 5′-biotin-labeled 601-bp dsDNA handles, PCR (polymerase chain reaction) amplification was performed using TaKaRa Ex Taq Polymerase (TaKaRa, China) with lambda phage DNA (Thermo Scientific, USA) as the template. The PCR products were purified using a Universal DNA Purification Kit (TIANGEN Biotech, China) and subsequently digested with the BstXI restriction enzyme (Thermo Scientific, USA). The oligonucleotides were phosphorylated and annealed with two flanking sequences and finally ligated with two dsDNA handles using T4 DNA ligase (TaKaRa, China). The ligated DNA products were analyzed by agarose gel electrophoresis and purified by gel extraction using a TIANgel Midi Purification Kit (TIANGEN Biotech, China).

Circular dichroism spectroscopy

Oligonucleotides were dissolved in a 10 mM Tris–HCl buffer (pH 8.0) containing 100 mM KCl at final concentrations of 2 or 5 μM for telomeric hairpin and G4-forming sequences, respectively. DNA samples were heated at 95°C for 5 min and then gradually cooled to 25°C. CD spectra were recorded us-

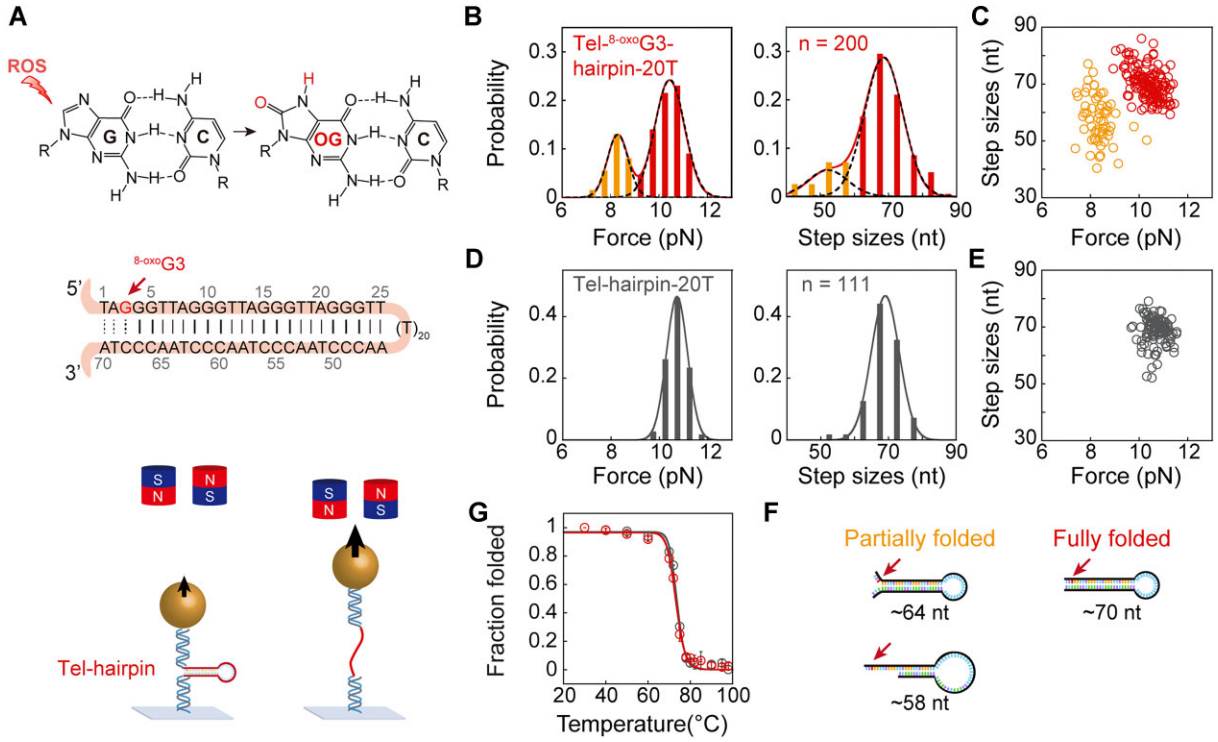

Figure 1. Mechanical and thermal stability of telomeric hairpin containing a single $^{8\text{-oxo}}$G. (**A**) Schematic of the magnetic tweezer measurements. Watson–Crick G-C and $^{8\text{-oxo}}$G-C base pair structures (top), Tel-$^{8\text{-oxo}}$G3-hairpin-20T sequence (middle), and magnetic tweezers (bottom). Unfolding force and step size distributions (**B**) and scatter plot (**C**) of Tel-$^{8\text{-oxo}}$G3-hairpin-20T. Data were fitted with a double Gaussian function. The major peak represents fully folded hairpins (red) and the minor peak represents partially folded hairpins (yellow). *n* represents the total number of unfolding events. Unfolding force and step size distributions (**D**) and scatter plot (**E**) of wild-type Tel-hairpin-20T. (**F**) Sketch models of possible partially folded hairpin structures of Tel-$^{8\text{-oxo}}$G3-hairpin-20T. (**G**) Circular dichroism (CD) melting curves of Tel-hairpin-20T (gray) and Tel-$^{8\text{-oxo}}$G3-hairpin-20T (red) were recorded at 270 nm in 100 mM KCl. Data were fitted with a sigmoidal model to obtain the T_m value.

ing a BioLogic MOS-500 spectropolarimeter in a 1-cm path-length quartz cuvette. Melting curves were obtained by monitoring the molar ellipticity at 270 nm (for hairpins) or 295 nm (for G4s) as the temperature was increased from 25°C to 98°C in 2–5°C increments, with 1-min equilibration time at each temperature. The melting temperatures were determined by fitting the normalized melting curves to a sigmoid function. A two-state model was employed to calculate thermodynamic parameters. By plotting ln $K_{eq}(T)$ against $1/T$, the enthalpy change (ΔH) and entropy change (ΔS) were determined from the slope ($-\Delta H/R$), and the *y*-intercept ($\Delta S/R$), respectively. The Gibbs free energy change (ΔG) was calculated using the equation $\Delta G = \Delta H - T\Delta S$ [36].

Single-molecule magnetic tweezers

BioPSI magnetic tweezers (BioPSI, Singapore) were used to conduct the experiments. A flow chamber was constructed on a coverslip modified with (3-aminopropyl)triethoxysilane (APTES) (Cool Chemical Technology, China). The thiol-labeled 5′-end of DNA constructs was covalently attached to the amine groups of the APTES-modified coverslip via a sulfo-SMCC cross-linker (Hunan HuaTeng Pharmaceutical, China). The flow chamber was blocked with bovine serum albumin (BSA) solution [10 mg/ml BSA (Sigma–Aldrich, China), 1 mM 2-mercaptoethanol, 1× phosphate saline buffer, pH 7.4]. Streptavidin-coated paramagnetic beads (Dynal M280, Thermo Fisher Scientific, USA) with a diameter of 2.8 μm were attached to the biotin-labeled 5′-end of the DNA construct. Additionally, 3-μm-diameter amino polystyrene particles (Baseline, China) were used as a reference bead to eliminate the drift of the sample channel. All experiments were performed at room temperature (22–26°C) in a buffer containing 10 mM Tris–HCl (pH 8.0) and 100 mM KCl buffer.

Data analysis

The unfolding force distributions of hairpins were fitted with Gaussian functions. The unfolding force distributions of G4s were analyzed using the Bell–Arrhenius model [37, 38], which describes the force-dependent unfolding rates as $k_u = k_{u0}\exp\left(\frac{\Delta x_u f}{k_B T}\right)$, where k_{u0} is the zero-force unfolding rate and Δx_u is the unfolding transition distance. The unfolding force distribution can be fitted using $p_{unfold}(f) = \frac{k_{u0}}{r}\exp\left\{\frac{\Delta x_u f}{k_B T} + \frac{k_B T k_{u0}}{\Delta x_u r}\left[1-\exp\left(\frac{\Delta x_u f}{k_B T}\right)\right]\right\}$ to obtain the k_{u0}. The folding free energies were determined based on the integration function [39]

$$\Delta G^0 = \int_0^{F_c} \Delta x\left(F'\right) dF', \quad (1)$$

where F_c is equilibrium critical force at which the probabilities of folded and unfolded states are equal, and $\Delta x(F)$ is the extension difference between unfolded (ssDNA) and folded (hairpin) states. The force–extension curves for single-stranded DNA (ssDNA) were described by the phenomenological relation proposed by Cocco *et al.* [40]. The lifetime histograms of folded states and unfolded states obtained at constant forces were analyzed using a custom MATLAB program as previously described [41]. Data were fitted with a single exponential decay function $A\exp(-kt)$, where k represents the

folding rate (k_f) or unfolding rate (k_u) under a specific force, where $\tau_u = 1/k_f$ and $\tau_f = 1/k_u$ denote the average lifetimes. For G4 structures, the folding free energy was determined by measuring the equilibrium constant K_{eq} and plotting $\ln(K_{eq})$ against force: $\ln(K_{eq}) = \frac{F\Delta x}{k_B T} + \frac{\Delta G^0}{k_B T}$; the zero-force free energy can be determined by extrapolating to zero force according to the Bell–Arrhenius model [37, 38, 42].

Results

Telomeric DNA hairpins containing a single $^{8\text{-oxo}}$G substitution can fold into different species with heterogeneous mechanical stability

We first used single-molecule magnetic tweezers to measure the unzipping forces of a 25-bp telomeric hairpin containing $(GGGTTA)_4$ repeat and a 20 thymine (20T) nucleotide loop, with or without a single $^{8\text{-oxo}}$G substitution (Tel-$^{8\text{-oxo}}$G3-hairpin-20T and Tel-hairpin-20T, respectively), using the force-ramp experiments. Figure 1A shows a schematic of a hairpin DNA molecule ligated to two dsDNA handles and tethered between a glass slide and a magnetic bead, as previously described [43]. In these force-ramp experiments, the force applied to DNA tethers was linearly increased from 1 to 60 pN at a constant loading rate of 2 pN/s to detect the unfolding events based on sudden jumps in bead height. Then, the force was rapidly jumped to 1 pN to allow hairpin refolding. Repeating these force-ramp cycles yielded the unfolding force and step sizes histograms, providing information on the mechanical stability and polymorphism of DNA structures. The observed unfolding step sizes of Tel-hairpin-20T suggests that the unfolded ssDNA predominantly folds into hairpin structures, rather than G4 structures [44] (Supplementary Fig. S1).

Figure 1B and C shows that Tel-$^{8\text{-oxo}}$G3-hairpin-20T exhibited two distinct unfolding force peaks: a major species (~70%) with an unfolding force of 10.4 ± 0.6 pN (mean ± standard deviation) and average step sizes of 69 ± 6 nucleotides (nt), and a minor species (~30%) with a lower unfolding force of 8.3 ± 0.4 pN and smaller step sizes of 52 ± 6 nt. In contrast, the wild-type Tel-hairpin-20T predominantly unfolded at a single unfolding force peak of 10.7 ± 0.4 pN and with step sizes of 69 ± 4 nt (Fig. 1D and E, and Table 1). The major folded species of Tel-$^{8\text{-oxo}}$G3-hairpin-20T displayed similar mechanical stability to the wild-type sequence. The presence of 30% minor species, characterized by a lower unfolding force and step size, suggests that a single $^{8\text{-oxo}}$G near the 5′-end of the hairpin can hinder the complete hairpin folding, leaving the first three bases of the stem unpaired or shifting GGGTTA repeats, which may generate minor species with smaller step sizes (Fig. 1F). However, previous optical tweezer experiments on a 29-bp hairpin revealed a predominant formation of partially folded hairpin driven by end fraying [27]. The Tel-$^{8\text{-oxo}}$G3-hairpin-20T primarily adopted a fully folded hairpin at 1 pN.

To further quantify the impact of $^{8\text{-oxo}}$G substitution on the thermal stability, we also performed CD melting measurements for Tel-$^{8\text{-oxo}}$G3-hairpin-20T and wild-type Tel-hairpin-20T (Fig. 1G and Supplementary Fig. S2). Both hairpins exhibited similar melting temperatures T_m: 73.1 ± 0.2°C (mean ± standard deviation) for Tel-$^{8\text{-oxo}}$G3-hairpin-20T and 73.7 ± 0.2°C for wild type. Consistent with this, van't Hoff analysis revealed comparable hybridization energies for both hairpins (−15.5 ± 0.9 kcal/mol for Tel-$^{8\text{-oxo}}$G3-hairpin-20T and −18 ± 1 kcal/mol for Tel-hairpin-20T, respectively) (Supplementary Table S2). These results were consistent with mechanical stability observed in magnetic tweezer experiments for the major folded species. These results indicate that a single $^{8\text{-oxo}}$G modification has a minimal impact on the overall hybridization energy of the fully folded telomeric hairpin. The T_m analysis is not sensitive to the minor population of partially folded hairpin intermediates.

Table 1. Unfolding forces of the telomeric hairpins measured by force-ramp experiments

Name	Unfolding force (pN)	Step sizes (nm)	Step sizes (nt)
Tel-hairpin-20T	10.7 ± 0.4	30 ± 1	69 ± 4
Tel-$^{8\text{-oxo}}$G3-hairpin-20T	10.4 ± 0.6	29 ± 2	69 ± 6
	8.3 ± 0.4	22 ± 3	52 ± 6
Tel-hairpin-4T	11.6 ± 0.4	23.6 ± 0.6	54 ± 1
Tel-$^{8\text{-oxo}}$G3-hairpin-4T	10.3 ± 0.4	20 ± 1	47 ± 2
Tel-$^{8\text{-oxo}}$G15-hairpin-4T	11.4 ± 0.3	23.6 ± 0.6	54 ± 1
Tel-$^{8\text{-oxo}}$G9-hairpin-4T	11.1 ± 0.3	23 ± 1	52 ± 2
Tel-$^{8\text{-oxo}}$G23-hairpin-4T	11.2 ± 0.3	23.0 ± 0.8	53 ± 1
Tel-G15-T-mismatch	9.9 ± 0.3	22.0 ± 0.7	53 ± 1
Tel-G3-T-mismatch	10.0 ± 0.6	20 ± 1	47 ± 2
Tel-G9-T-mismatch	9.9 ± 0.4	14.9 ± 0.8	36 ± 2

An $^{8\text{-oxo}}$G substitution near the 5′-end causes significant end-fraying effects and hinders the complete folding of telomeric hairpin with 4-nt loop

To investigate whether the position of $^{8\text{-oxo}}$G influences the formation of partially folded hairpin structures (end fraying), we designed additional telomeric hairpin constructs: Tel-$^{8\text{-oxo}}$G3-hairpin-4T and Tel-$^{8\text{-oxo}}$G15-hairpin-4T (Supplementary Table S1). A 4 thymine (4T) nucleotide loop was incorporated to accelerate folding kinetics comparing to 20-nt loop and facilitate the observation of equilibrium folding/unfolding transitions. $^{8\text{-oxo}}$G3 and $^{8\text{-oxo}}$G15 indicate $^{8\text{-oxo}}$G modification near the 5′-end and in the middle of the hairpin, respectively. The stretching curves of the hairpin with a 20-nt loop (Tel-$^{8\text{-oxo}}$G3-hairpin-20T) showed sudden extension jump, indicating measurements far from equilibrium, whereas the 4-nt loop hairpin (Tel-$^{8\text{-oxo}}$G3-hairpin-4T) was near equilibrium, as evidenced by reversible folding/unfolding transitions (Fig. 2A and Supplementary Fig. S3). The unfolding force histograms of Tel-$^{8\text{-oxo}}$G3-hairpin-4T revealed a single unfolding force peak with lower force (10.3 ± 0.4 pN) and smaller step sizes (47 ± 2 nt), compared to the wild-type Tel-hairpin-4T (11.6 ± 0.4 pN and 54 ± 1 nt, respectively) (Fig. 2B and C). This suggests that Tel-$^{8\text{-oxo}}$G3-hairpin-4T predominantly forms partially folded hairpins with lower unzipping forces and smaller step sizes than wild type. Tel-$^{8\text{-oxo}}$G3-hairpin-4T exhibits stronger end-fraying effects than Tel-$^{8\text{-oxo}}$G3-hairpin-20T, despite the identical $^{8\text{-oxo}}$G position, suggesting that the end-fraying effects result from hindered rehybridization by $^{8\text{-oxo}}$G under forces (~10 pN). Similarly, when $^{8\text{-oxo}}$G was positioned near the 3′-end of reverse sequence (Tel-$^{8\text{-oxo}}$G52-hairpin-4T), comparable end-fraying phenomena were also observed (Supplementary Fig. S4). This observation explains why a previous study, using a 29-bp hairpin with a 6-nt loop and two $^{8\text{-oxo}}$G near the 5′-end, also reported significant end-fraying effects [27].

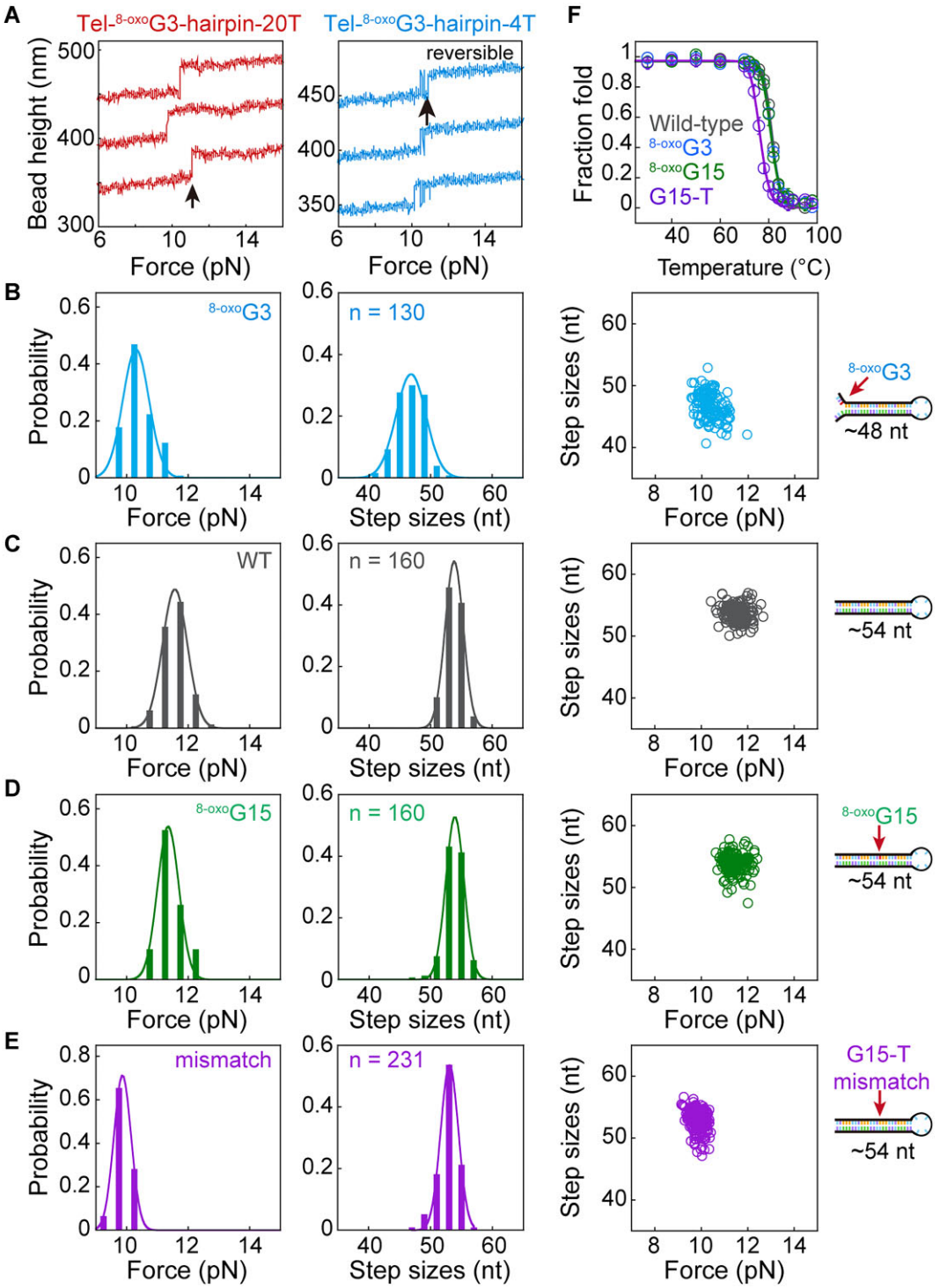

Figure 2. Effects of an 8-oxoG substitution on unfolding forces of telomeric DNA hairpins. (**A**) Representative unfolding curves of Tel-8-oxoG3-hairpin-20T and Tel-8-oxoG3-hairpin-4T recorded in 100 mM KCl buffer at a loading rate of 2 pN/s. The hairpins with 20T and 4T loops exhibit irreversible and reversible unfolding transitions, respectively. (**B**-**E**)Unfolding force and step sizes of Tel-8-oxoG3-hairpin-4T (**B**), Tel-hairpin-4T (**C**), Tel-8-oxoG15-hairpin-4T (**D**), and Tel-G15-T-mismatch (**E**). Left panel: unfolding force distributions; middle panel: unfolding step size distributions; right panel: scatter plots. The unfolding force and step size distributions were fitted with the Gaussian function. (**F**) CD melting curves of Tel-hairpin-4T (wild type), Tel-8-oxoG3-hairpin-4T (8-oxoG3), Tel-8-oxoG15-hairpin-4T (8-oxoG15), and Tel-G15-T-mismatch (G15-T). Data were fitted by using a sigmoidal model.

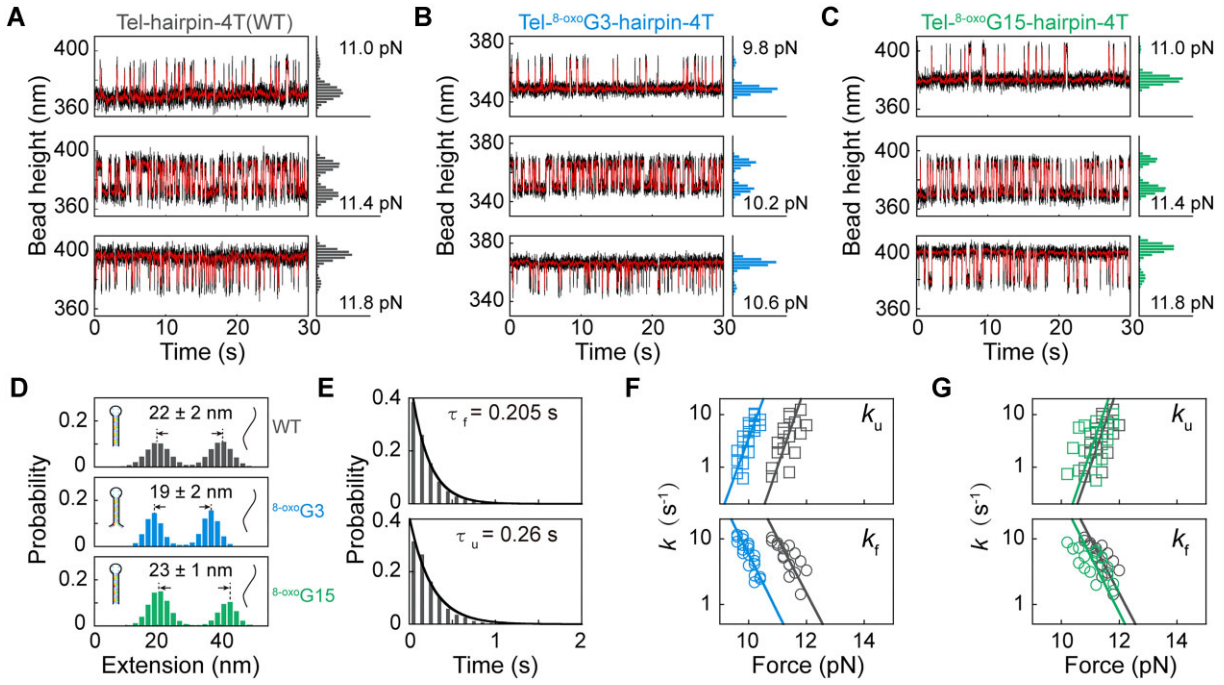

Figure 3. Equilibrium folding and unfolding dynamics of telomeric hairpins under constant forces. Representative time traces of Tel-hairpin-4T (**A**), Tel-$^{8\text{-oxo}}$G3-hairpin-4T (**B**), and Tel-$^{8\text{-oxo}}$G15-hairpin-4T (**C**) were recorded at constant forces. The red lines show smoothed time traces. Histograms of the probability are alongside the trajectories. (**D**) The distance between folded and unfolded hairpins near critical forces. The marked extension changes are average from four individual DNA molecules. (**E**) Dwell time analysis of Tel-hairpin-4T at 11.5 pN. Data were collected from four individual DNA molecules. (**F**, **G**) Force-dependent unfolding rates (k_u) and folding rates (k_f) of Tel-hairpin-4T (gray), Tel-$^{8\text{-oxo}}$G3-hairpin-4T (blue), and Tel-$^{8\text{-oxo}}$G15-hairpin-4T (green). Data were fitted by the Bell–Arrhenius model.

In contrast to the lesion located near the 5′-end, Tel-$^{8\text{-oxo}}$G15-hairpin-4T with an $^{8\text{-oxo}}$G lesion at the hairpin midpoint exhibited a similar unfolding force peak (11.4 ± 0.3 pN) and step size (54 ± 1 nt) to the wild-type Tel-hairpin-4T (Fig. 2C and D). Furthermore, when $^{8\text{-oxo}}$G lesions were introduced at additional internal positions (Tel-$^{8\text{-oxo}}$G9-hairpin-4T and Tel-$^{8\text{-oxo}}$G23-hairpin-4T), similar mechanical behaviors were observed (Supplementary Fig. S5). Collectively, these results suggest that $^{8\text{-oxo}}$G modification in the middle of a 25-bp hairpin has a minimal impact on hairpin structural integrity and mechanical stability comparing with wild-type sequence, consistent with previous X-ray and NMR structural studies [24, 25]. The similar unfolding forces and step sizes between Tel-$^{8\text{-oxo}}$G15-hairpin-4T and wild-type hairpin indicate comparable hybridization energy. The folding free energy ΔG_0 was calculated using the equation $\Delta G^0 = -\int_0^{Fc} \Delta x(F)\mathrm{d}F$, yielding values of $-40\ k_BT$ and $-41\ k_BT$ for Tel-$^{8\text{-oxo}}$G15-hairpin-4T and wild-type Tel-hair-4T, respectively (see the "Materials and methods" section and Supplementary methods) [39]. We utilized average unfolding force for each sequence to calculate F_c, because the reversible folding/unfolding signal suggests that the unfolding forces were very close to F_c. To further compare the stability of $^{8\text{-oxo}}$G-C base pairs with other DNA lesions, we also measured the unzipping force of a telomeric hairpin containing a single G-T mismatch (Tel-G15-T-mismatch) using the same force-ramp procedure. In contrast to $^{8\text{-oxo}}$G, a single G-T mismatch located at the center of the 25-bp telomeric hairpin significantly decreased the average unzipping force to 9.9 ± 0.3 pN and the hybridization energy to $\Delta G_{folding} = -32\ k_BT$ (19 kcal/mol), while the unfolding step sizes remained 53 ± 1 nt (Fig. 2E). CD melting experiments revealed that the T_m values of Tel-$^{8\text{-oxo}}$G3-hairpin-4T and Tel-$^{8\text{-oxo}}$G15-hairpin-4T were consistent with that of the wild type, while Tel-G15-T-mismatch showed a significantly lower T_m ($\Delta T_m = 4.9°C$) compared to the wild type (Fig. 2F and Supplementary Table S3). Placing the mismatch near 5′-end (Tel-G3-T-mismatch and Tel-G9-T-mismatch) resulted in significant reduction of unfolding step sizes and unfolding forces, suggesting that a mismatch near the 5′-end also induced end-fraying effects in directional force unzipping (Supplementary Fig. S6). These results suggest that a G-T mismatch has a more pronounced destabilizing effect on the hairpin compared to the $^{8\text{-oxo}}$G-C base pair.

Force-dependent folding/unfolding rates of $^{8\text{-oxo}}$G-substituted telomeric hairpin measured at constant forces

To accurately determine the hybridization energy and folding/unfolding dynamics, we further conducted constant force measurements. Figure 3A presents representative trajectories of Tel-hairpin-4T held at three different constant stretching forces. At a low force (11.0 pN), the DNA molecule predominantly resides in the folded states. As the stretching force increases, the equilibrium shifts toward the unfolded state, with the unfolded state becoming dominant at 11.8 pN. At a force of ∼11.4 pN, the probabilities of the molecule being in the folded and unfolded states are equal, indicating that this force is close to the critical force (F_c). We fitted the histogram of bead height with two Gaussian functions to determine the equilibrium constant $K_{eq} = P_{unfold}/P_{fold}$, for the unfolding reaction (Fig. 3A, right panel). By plotting $\ln(K_{eq})$ against force and fitting the data with $\ln(K_{eq}) = \frac{F\Delta x}{k_BT} + \frac{\Delta G^0}{k_BT}$, we determined F_c to be 11.4 ± 0.3 pN, where $\ln(K_{eq})$ equals zero. The value

Table 2. Effects of $^{8\text{-oxo}}$G on folding free energy of the telomeric hairpins measured under constant forces

Name	F_c (pN)	Step sizes (nm)	ΔG (k_BT)[a]
Tel-hairpin-4T	11.4 ± 0.3	22 ± 2	−40 ± 2
Tel-$^{8\text{-oxo}}$G3-hairpin-4T	10.1 ± 0.1	19 ± 2	−29 ± 1
Tel-$^{8\text{-oxo}}$G15-hairpin-4T	11.2 ± 0.5	23 ± 1	−39 ± 3

[a] 1 $k_BT \approx 0.593$ kcal/mol at 25°C.

is consistent with the force-ramp experiments shown in Fig. 2C. We estimated the folding free energy $\Delta G^0 = -63 \pm 4$ k_BT (37 kcal/mol) by linearly extrapolating the function to zero force (Supplementary Fig. S7). However, for long hairpins, this method can overestimate the ΔG^0 due to the force–extension behavior of the unfolded ssDNA. Therefore, we determined the folding free energy ΔG^0 using the integral equation $\Delta G^0 = -\int_0^{F_c} \Delta x(F)dF$, utilizing the experimentally measured force–extension curve of ssDNA (the "Materials and methods" section and equation 1) [39]. This analysis yielded a free energy of –40 ± 2 k_BT (23.7 kcal/mol) for Tel-hairpin-4T, which is in good agreement with the hybridization energy analyzed using the Mfold web server (29.95 kcal/mol) (Supplementary Fig. S8). It should be noted that the Mfold currently lacks the necessary parameters for $^{8\text{-oxo}}$G lesions.

For Tel-$^{8\text{-oxo}}$G3-hairpin-4T with $^{8\text{-oxo}}$G near 5′-end, the critical force F_c, determined by linear fitting $\ln(K_{eq})$ versus force, was 10.1 ± 0.1 pN, significantly lower than that of wild-type Tel-hairpin 4T (11.4 ± 0.3 pN) (Fig. 3B). In contrast, Tel-$^{8\text{-oxo}}$G15-hairpin-4T, containing a midpoint located $^{8\text{-oxo}}$G, exhibited a critical force (11.2 ± 0.5 pN) similar to that of the wild-type sequence (Fig. 3C and Table 2). The folding free energy calculated using $\Delta G^0 = -\int_0^{F_c} \Delta x(F)dF$ was −29 ± 1 k_BT (17 kcal/mol) for Tel-$^{8\text{-oxo}}$G3-hairpin-4T and −39 ± 3 k_BT (23 kcal/mol) for Tel-$^{8\text{-oxo}}$G15-hairpin-4T (Table 2). Furthermore, the unfolding step size of Tel-$^{8\text{-oxo}}$G3-hairpin-4T (Δx = 19 ± 2 nm) measured at F_c was significantly lower than that of Tel-hairpin-4T (22 ± 2 nm) and Tel-$^{8\text{-oxo}}$G15-hairpin-4T (23 ± 1 nm) (Fig. 3D and Table 2). The reduced unfolding step sizes for Tel-$^{8\text{-oxo}}$G3-hairpin-4T are consistent with the force-ramp results, suggesting that the $^{8\text{-oxo}}$G modification near the 5′-end disrupts hairpin refolding under force, leading to the formation of partially folded structure and the observed end-fraying effects at critical forces.

Subsequently, we estimated folding/unfolding kinetics of hairpins by analyzing the dwell times from the constant force measurements. Dwell time histograms for both states were fitted to a single exponential function $P = A\exp(-t/\tau)$ (Fig. 3E). The unfolding rate k_u and folding rate k_f were extracted from these fits, with their reciprocal ($\tau = 1/k$) representing the unfolding and folding lifetimes. At the critical force of 11.5 pN for Tel-hairpin-4T, the values of τ_u and τ_f were 0.205 ± 0.004 s and 0.26 ± 0.01 s (average ± fitting error), respectively (Fig. 3E). These values represent the average data collected from at least four independent tethers. Next, we analyzed the force-dependent k_u and k_f for Tel-hairpin-4T, Tel-$^{8\text{-oxo}}$G3-hairpin-4T, and Tel-$^{8\text{-oxo}}$G15-hairpin-4T (Fig. 3F and G) and the data were fitted by Bell–Arrhenius fitting. Tel-hairpin-4T and Tel-$^{8\text{-oxo}}$G3-hairpin-4T exhibit significant differences in k_f and k_u (Fig. 3F), while no significant differences were observed between Tel-hairpin-4T and Tel-$^{8\text{-oxo}}$G15-hairpin-4T (Fig. 3G). Notably, at a force of 10.1 pN, near the critical force F_c, k_u of Tel-$^{8\text{-oxo}}$G3-hairpin-4T (5.1 s^{-1}) was 130 times higher than that of Tel-hairpin-4T (k_u = 0.039 s^{-1}). These findings suggest that the end-fraying effects caused by $^{8\text{-oxo}}$G modification significantly accelerate the unfolding rate and reduce the refolding rate, particularly at forces near the critical forces.

An $^{8\text{-oxo}}$G substitution at the 5′-end of G4s reduced the unfolding force and Hoogsteen hydrogen bonding of telomeric G4s

A recent optical tweezer study has shown that $^{8\text{-oxo}}$G substitution within the middle of G-tetrads can reduce the unfolding force of human telomeric G4 from 21.7 to 18.9 pN [34]. However, the $^{8\text{-oxo}}$G at the 5′-end of telomeric G4s remains unexplored. Hence, we also quantified the unfolding force of 5′-G-modified G4s using force-ramp experiments as previously described [41] (Fig. 4A–C). The unfolding force distribution of Tel-$^{8\text{-oxo}}$G3-G4 showed a major peak at 12 ± 4 pN (n = 159), significantly lower than that of wild-type Tel-G4 (16 ± 6 pN) (Fig. 4D). Using the Bell–Arrhenius model, we determined the unfolding rates k_u for Tel-$^{8\text{-oxo}}$G3-G4 and wild-type Tel-G4 structures. The best-fitting parameter for zero-force unfolding rate (k_{u0}) of the Tel-$^{8\text{-oxo}}$G3-G4 was k_{u0} = 0.020 ± 0.001 s^{-1}, while for wild-type Tel-G4, k_{u0} was 0.009 ± 0.008 s^{-1}, indicating that the $^{8\text{-oxo}}$G substitution increased the zero-force unfolding rates of G4s. Fitted with a single Gaussian peak, the unfolding step size of wild-type Tel-G4 was 21 ± 4 nt, consistent with its full length (Fig. 4E). In contrast, the $^{8\text{-oxo}}$G-substituted telomeric G4s showed a single peak at 19 ± 3 nt (Table 3). The significant reduction of step sizes and unfolding forces suggests that the 5′-end $^{8\text{-oxo}}$G modification destabilized the G4 structure, leading to weakened Hoogsteen hydrogen bonding resulting in the formation of less stable G4 structures. The partially folded guanine-vacancy G4s have also been observed in the NMR structure of 3′-end $^{8\text{-oxo}}$G-modified Bloom syndrome protein (BLM) promoter G4s [45].

Next, we analyzed the time-dependent folding probability $P_{fold}(t)$ for 5′-end $^{8\text{-oxo}}$G-modified telomeric G4s as previously reported [41] (Fig. 4F). The saturation folding probability reduced from 89% to 74% (Fig. 4F). Using exponential function, $P_{fold}(t) = P_{st} * \frac{k_f}{k_f+k_u}[1-\exp(-(k_f+k_u)t)]$, we obtained the folding and unfolding rates of k_f= 0.15 ± 0.07 s^{-1} and k_u = 0.03 ± 0.03 s^{-1}, respectively. The folding rates for the Tel-$^{8\text{-oxo}}$G3-G4 were one order of magnitude smaller than the Tel-G4 (k_f = 1.0 ± 0.2 s^{-1}) [41], suggesting that 5′-end oxidized guanines can markedly reduce formation of stable G4s.

The significant reduction of unfolding force and folding rate of Tel-$^{8\text{-oxo}}$G3-G4 was consistent with previous thermodynamic measurements of $^{8\text{-oxo}}$G-substituted telomeric G4s using CD spectroscopy [10, 11]. We also performed CD measurements and the spectra of Tel-$^{8\text{-oxo}}$G3-G4 in 100 mM K^+ buffer display a minimum at ∼260 nm and a maximum at ∼295 nm, which differ from the wild-type Tel-G4 in both 100 mM K^+ and 100 mM Na^+, suggesting that $^{8\text{-oxo}}$G may induce a structural transition (Fig. 4G) [10, 12. The melting temperatures of Tel-$^{8\text{-oxo}}$G3-G4 and wild-type Tel-G4 are ∼47°C and 62°C, respectively, which is consistent with previous measurements (Fig. 4H) [10]. The calculated apparent values for ΔH, ΔS, and ΔG were found to be −54 ± 2 kcal/mol, −162 ± 6 cal K/mol, and −5.9 ± 0.3 kcal/mol for the Tel-G4, and −47 ± 1 kcal/mol, −147 ± 5 cal K/mol, and −3.3 ± 0.1 kcal/mol for the Tel-$^{8\text{-oxo}}$G3-G4, respectively (Supplementary Table S4). These values were in good agreement with previous CD mea-

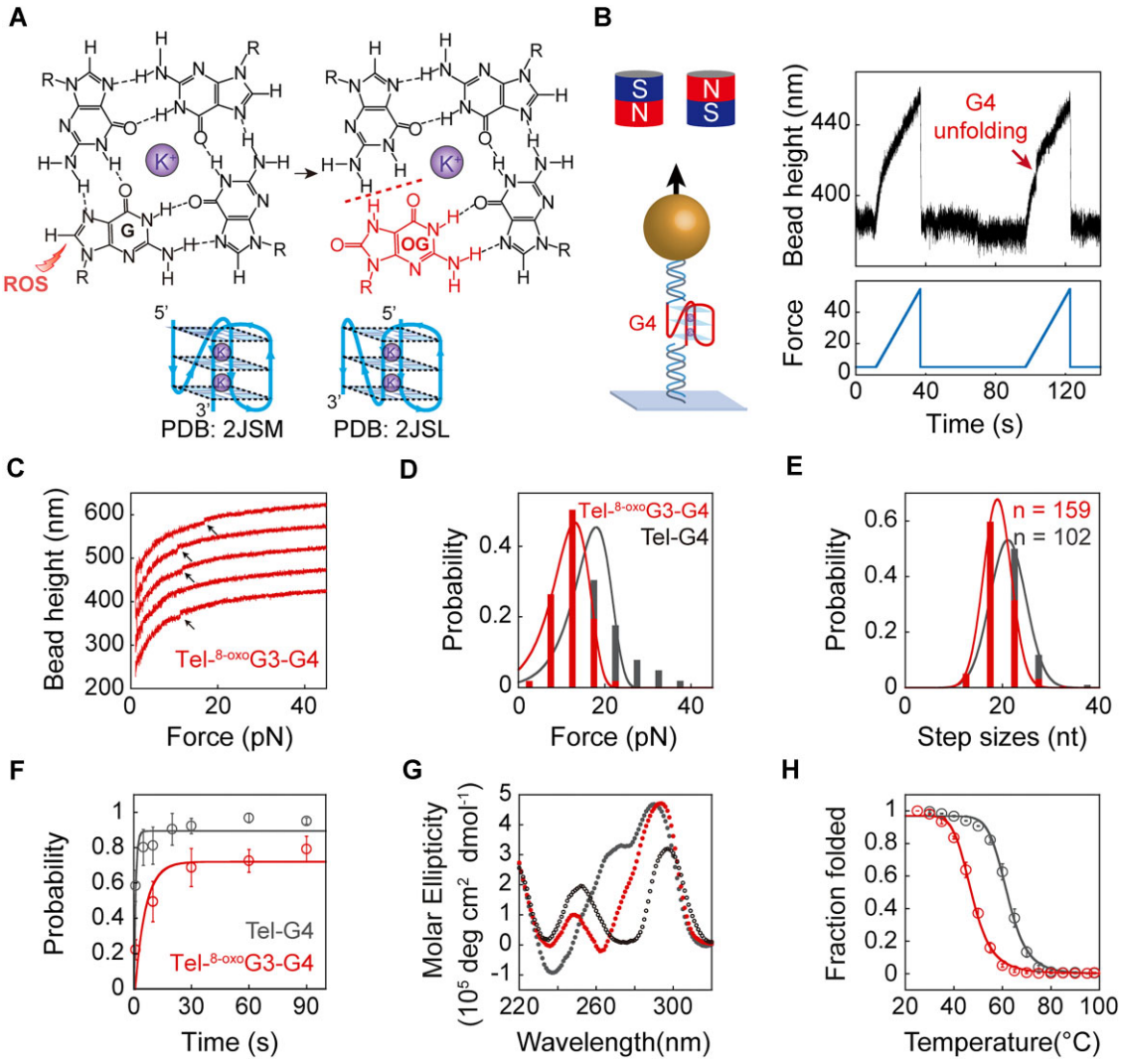

Figure 4. Effects of an $^{8\text{-oxo}}$G modification at the 5′-end on the mechanical and thermal stability of telomeric G4. (**A**) Structures of G-tetrad (top, left) and its oxidized structures (top, right). Hydrogen at the C8 position is replaced by oxygen and protonation at the N7 position affects the Hoogsteen hydrogen bond formation. Two hybrid topologies of telomeric G4 structures are placed below the G-tetrad. (**B**) Magnetic tweezer experiment for G4s (left) and force-ramp procedures (right). The Tel-$^{8\text{-oxo}}$G3-G4 sequence is between two dsDNA handles. Arrows represent the G4 unfolding signals. (**C**) Typical bead height traces of Tel-$^{8\text{-oxo}}$G3-G4 during repeated stretching cycles. The curves are shifted along the bead height axis for visual clarity. (**D**) Unfolding force histograms. Data were fitted by the Bell–Arrhenius model. (**E**) Unfolding step size distributions. Data were fitted by the Gaussian function. *n* represents the total number of unfolding events. (**F**) The time evolution of the folding probability $p_{fold}(t)$ of Tel-$^{8\text{-oxo}}$G3-G4 and Tel-G4. Data were fitted by an exponential function. (**G**) CD spectra of Tel-$^{8\text{-oxo}}$G3-G4 (red) and wild-type Tel-G4 (gray) in 100 mM KCl, and Tel-G4 in 100 mM NaCl (black open cycles) measured at 25°C. Data were recorded at 295 nm in the presence of 100 mM KCl. (**H**) CD melting curves of Tel-$^{8\text{-oxo}}$G3-G4 (red) and Tel-G4 (gray), with error bars indicating the standard deviations from three measurements. Data were fitted by using a sigmoidal model.

surements in 169 mM KCl concentration [10]. The change in the enthalpy for G4s melting also suggests that $^{8\text{-oxo}}$G significantly reduced hydrogen bond formation.

Force-dependent folding/unfolding rates of $^{8\text{-oxo}}$G-substituted telomeric G4s measured at constant forces

To investigate the effects of $^{8\text{-oxo}}$G lesion on the folding/unfolding dynamics of telomeric G4, we measured the Tel-$^{8\text{-oxo}}$G3-G4 under constant forces from 3 to 5 pN (Fig. 5A). At 3 pN, Tel-$^{8\text{-oxo}}$G3-G4 mostly formed a folded state, and at 4 pN, it almost reached a balance between folded and unfolded states, while at 5 pN, it turned out to be an unfolded state in majority (Fig. 5A). The histograms depicting the extension of Tel-$^{8\text{-oxo}}$G3-G4 were fitted with two Gaussian functions, showing the corresponding folding/unfolding transition at different forces (Fig. 5A).

Table 3. Comparisons of $^{8\text{-oxo}}$G substitution and wild-type telomeric G4s

Name	Unfolding force (pN)	Step sizes (nm)	Step sizes (nt)	F_c (pN)	ΔG (k_BT)
Tel-G4 (wild type)	16 ± 6	8 ± 2	21 ± 4	5.7	−5.9
Tel-$^{8\text{-oxo}}$G3-G4	12 ± 4	7 ± 1	19 ± 3	3.3	−2.3

Figure 5B shows the lifetime histograms of Tel-$^{8\text{-oxo}}$G3-G4 folded state and unfolded state obtained at 5 pN. The lifetime histogram in unfolded state of Tel-$^{8\text{-oxo}}$G3-G4 was fitted with a single exponential decay, yielding an average lifetime $\tau_{u,5\ pN}$= 27 ± 2 s for Tel-$^{8\text{-oxo}}$G3-G4. This lifetime was longer than that of wild-type Tel-G4 (15.8 ± 0.4 s) previ-

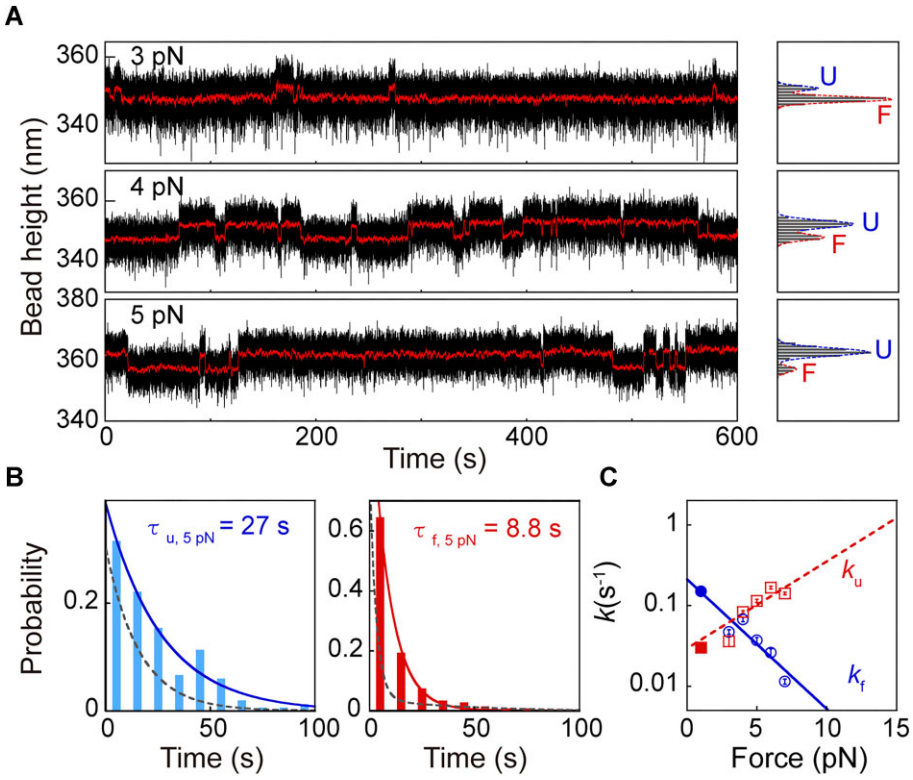

Figure 5. Equilibrium folding/unfolding dynamics of Tel-$^{8\text{-oxo}}$G3-G4. (**A**) Representative folding and unfolding trajectories of Tel-$^{8\text{-oxo}}$G3-G4 were measured at 3 pN (top), 4 pN (middle), and 5 pN (bottom). Red line represents the smoothed data. U represents the unfolded states and F represents the folded states. (**B**) Dwell time of Tel-$^{8\text{-oxo}}$G3-G4 at 5 pN, which is fitted by a single exponential decay function yielding time constants of $\tau_{u,5\ pN} = 27$ s and $\tau_{f,5\ pN} = 8.8$ s. Data were collected from at least three independent tethers and were aggregated at each force. The gray dashed lines in these figures represent the dwell time of Tel-G4 at 5 pN, with data retrieved from a previously published study [41]. (**C**) Force-dependent folding rates (k_f) and unfolding rates (k_u) of Tel-$^{8\text{-oxo}}$G3-G4 fitted by the Bell–Arrhenius model.

ously measured under the same buffer condition and force [41], suggesting that the $^{8\text{-oxo}}$G modification reduced the folding rates of G4s, consistent with force-ramp measurements. The lifetime of the folded state can also be fitted with a single exponential decay with $\tau_{f,5\ pN} = 8.8 \pm 0.4$ s. These results suggest that the folding/unfolding dynamics of Tel-$^{8\text{-oxo}}$G3-G4 can be analyzed as a simple two-state model separated by a single energy barrier. In contrast, the wild-type telomeric G4s in the same 100 mM KCl buffer condition can fold into multiple structures with different lifetimes (short-lived state $\tau_{f,5\ pN} = 3.0$ s, long-lived state $\tau_{f,5\ pN} = 45$ s, and ultra-long-lived state >100 s) [41]. The average lifetime of $^{8\text{-oxo}}$G-modified G4s was longer than that of the short-lived state (intermediate) but shorter than that of the long-lived state (fully folded hybrid stranded G4s) [41]. This result suggests that $^{8\text{-oxo}}$G modification at 5′-end can reduce the lifetime of G4s compared with fully folded G4s. Figure 5C shows the force-dependent folding rate k_f ($1/\tau_u$) and unfolding rates k_u ($1/\tau_f$). Both k_u and k_f were analyzed using the Bell–Arrhenius model, yielding parameters $k_{u0} = 0.03 \pm 0.01\ s^{-1}$ and $\Delta x_u = 1.5 \pm 0.3$ nm, $k_{f0} = 0.21 \pm 0.03\ s^{-1}$ and $\Delta x_f = 1.0 \pm 0.3$ nm. The critical force F_c determined by the condition $k_u = k_f$, was found to be 3.3 pN for Tel-$^{8\text{-oxo}}$G3-G4, significantly lower than that of wild-type G4s ($F_c \sim 5.7$ pN) [41], suggesting a significant decrease in folding energy of G4s upon single $^{8\text{-oxo}}$G substitution. The zero-force folding free energy of G4 was determined by linear extrapolation $\ln(K_{eq}) = \frac{F\Delta x}{k_B T} + \frac{\Delta G^0}{k_B T}$ to zero force. This analysis yielded values of $-2.3\ k_B T$ (-1.4 kcal/mol) for Tel-$^{8\text{-oxo}}$G3-G4 and $-5.9\ k_B T$ (-3.5 kcal/mol) for Tel-G4 (Supplementary Fig. S9 and Table 3). The significant reduction of folding energy is also consistent with the CD melting measurements (Supplementary Fig. S10).

Discussion

In the current study, we first showed that a single $^{8\text{-oxo}}$G can result in telomeric hairpin (Tel-$^{8\text{-oxo}}$G3-hairpin-20T) forming different structural species with heterogeneous mechanical stability. Through both force-ramp and constant force measurements, we quantified the force-dependent unfolding and folding rates and folding free energy of wild-type and modified hairpins. We showed that a single $^{8\text{-oxo}}$G near the unzipping terminus (5′-end or 3′-end) can prevent complete refolding of the hairpin (Figs 2 and 3, and Supplementary Fig. S4). When sugjected to ∼10.1 pN force, the Tel-$^{8\text{-oxo}}$G3-hairpin-4T construct exhibited a 130-fold increase in hairpin unfolding rates. The significant change of unzipping kinetics induced by a single $^{8\text{-oxo}}$G has also been analyzed using nanopore ion channel α-hemolysin [22]. In contrast to $^{8\text{-oxo}}$G located near the 5′-end, an $^{8\text{-oxo}}$G-C base pair located at the middle of the hairpin (Tel-$^{8\text{-oxo}}$G15-hairpin-4T) did not significantly destabilize DNA; the change in hybridization energy was $<2\ k_B T$ for a single $^{8\text{-oxo}}$G.

It is important to note that our single-molecule experiments apply a directional force to unzip the hairpin, which accounts for the observed differences between $^{8\text{-oxo}}$G located at the 5′-

end and in the middle of the sequence. Directional unzipping is physiologically significant because it mimics the directional movement of replication forks, revealing the significant impact of $^{8\text{-oxo}}$G lesion. Specifically, an $^{8\text{-oxo}}$G lesion near the 5′-end dramatically increased (∼130-fold) hairpin unzipping rates under forces, providing valuable insights into how $^{8\text{-oxo}}$G lesions may affect replication fidelity. The end-fraying effects of $^{8\text{-oxo}}$G may also facilitate its recognition of $^{8\text{-oxo}}$G by DNA damage repair enzymes such as human OGG1 (8-oxo guanine DNA glycosylase). OGG1 can specifically recognize and remove $^{8\text{-oxo}}$G from duplex DNA initiating the base excision repair pathway [46, 47].

The destabilization of the $^{8\text{-oxo}}$G-C base pair in the middle was much insignificant compared with the G-T mismatch as a single G-T mismatch at the middle of the hairpin significantly reduced the unfolding forces. Our results suggest that $^{8\text{-oxo}}$G lesions located in the long duplex can maintain integrity and stability similar to normal Watson–Crick base pairing. These results are consistent with previous structural studies that the hydrogen bonds and stacking in the $^{8\text{-oxo}}$G-C base pair are highly similar to those in undamaged G-C base pair. These values can help to refine the NN parameters for $^{8\text{-oxo}}$G-modified nucleotides. Because DNA hybridization is also widely used in DNA nanobiotechnology [48], the accurate quantification of base-pairing energy also has implication in the design of DNA nanodevices that can respond to oxidative stress.

Through constant force measurements, we directly measured the equilibrium folding/unfolding transition of Tel-$^{8\text{-oxo}}$G3-G4 and the hairpin at physiologically relevant K^+ concentration. The decrease in folding rates of G4s by substitution of guanine with $^{8\text{-oxo}}$G has also been observed for tetramolecular G4s [49]. Previous studies using nanopore technology have demonstrated that the $^{8\text{-oxo}}$G substitution can result in a 10-fold increase in the unfolding rates of telomeric G4 in the presence of 100 mM NaCl [32]. However, nanopore techniques have difficulty in detecting the unfolding of these stable G4 structures that have slow unfolding rates, such as telomeric G4s at the physiological level of 100 mM KCl [32]. Our results revealed that a single $^{8\text{-oxo}}$G substitution at 5′-end significantly increased the unfolding rate (from $k_u = 0.009 \pm 0.008\ s^{-1}$ for wild type to $k_u = 0.020 \pm 0.001\ s^{-1}$ for Tel-$^{8\text{-oxo}}$G3-G4) and significantly decreased G4 folding energy (from 5.9 k_BT to 2.3 k_BT). Previous optical tweezer study has shown that an $^{8\text{-oxo}}$G substitution in the middle of G-tetrads significantly reduced the folding probability and the unfolding force of human telomeric G4s [34]. This observation combined with our results of 5′-end substitution suggests that $^{8\text{-oxo}}$G substitution exerts a more pronounced destabilizing effect on G4s compared to duplexes. The difference in destabilization can be attributed to the distinct impact of $^{8\text{-oxo}}$G on hydrogen bonding (Fig. 4A). In hairpin structures, $^{8\text{-oxo}}$G does not alter the overall number of hydrogen bonds (Fig. 1A). However, in G4s, $^{8\text{-oxo}}$G leads to a loss of two hydrogen bonds, thus explaining the observed difference.

Destabilizing telomeric G4 stability and downregulating the folding/unfolding kinetics can enhance the accessibility of telomerase [6] and telomere-binding protein POT1 [33], thereby maintaining the telomeric overhang. Notably, telomeres undergo shortening throughout the human lifespan and are thus often described as a molecular clock for assessing cellular age. In addition, studies recently demonstrated that $^{8\text{-oxo}}$G participates in the telomerase activities [50]. Consequently, quantifying the impact of $^{8\text{-oxo}}$G lesions on the stability and folding/unfolding kinetics of duplexes and G4s would significantly enhance our understanding of the effects of oxidative stress on telomere regions *in vivo*.

Acknowledgements

The authors thank Xinghua Zhang for the stimulating discussions.

Author contributions: Yuanlei Cheng (Data curation [equal], Formal analysis [equal], Funding acquisition [equal], Investigation [equal], Methodology [equal], Supervision [supporting], Validation [equal], Visualization [equal], Writing—original draft [equal], Writing—review & editing [equal]), Ximin Wang (Data curation [equal], Investigation [equal], Methodology [equal], Visualization [equal], Writing—original draft [equal]), Xuyang Yang (Investigation [supporting], Methodology [supporting]), Yashuo Zhang (Data curation [supporting], Investigation [supporting], Methodology [supporting], Writing—review & editing [supporting]), and Huijuan You (Conceptualization [lead], Funding acquisition [equal], Investigation [supporting], Methodology [supporting], Project administration [lead], Supervision [lead], Validation [equal], Visualization [supporting], Writing—original draft [lead], Writing—review & editing [lead]).

Supplementary data

Supplementary data is available at NAR Online.

Conflict of interest

None declared.

Funding

This work was supported by the National Natural Science Foundation of China (32171225 and 32301032) and the Wuhan Science and Technology Bureau (2023020201020542). Funding to pay the Open Access publication charges for this article was provided by National Natural Science Foundation of China.

Data availability

The data underlying this article are available in the article and in its online supplementary material.

References

1. Tubbs A, Nussenzweig A. Endogenous DNA damage as a source of genomic instability in cancer. *Cell* 2017;**168**:644–56. https://doi.org/10.1016/j.cell.2017.01.002
2. Seidel CAM, Schulz A, Sauer MHM. Nucleobase-specific quenching of fluorescent dyes. 1. Nucleobase one-electron redox potentials and their correlation with static and dynamic quenching efficiencies. *J Phys Chem* 1996;**100**:5541–53. https://doi.org/10.1021/jp951507c
3. Wu JZ, McKeague M, Sturla SJ. Nucleotide-resolution genome-wide mapping of oxidative DNA damage by click-code-seq. *J Am Chem Soc* 2018;**140**:9783–7. https://doi.org/10.1021/jacs.8b03715

4. Lim CJ, Cech TR. Shaping human telomeres: from shelterin and CST complexes to telomeric chromatin organization. *Nat Rev Mol Cell Biol* 2021;**22**:283–98. https://doi.org/10.1038/s41580-021-00328-y
5. Fleming AM, Burrows CJ. Oxidative stress-mediated epigenetic regulation by G-quadruplexes. *NAR Cancer* 2021;**3**:zcab038. https://doi.org/10.1093/narcan/zcab038
6. Fouquerel E, Lormand J, Bose A *et al.* Oxidative guanine base damage regulates human telomerase activity. *Nat Struct Mol Biol* 2016;**23**:1092–100. https://doi.org/10.1038/nsmb.3319
7. Wang Y, Patel DJ. Solution structure of the human telomeric repeat d[$AG_3(T_2AG_3)_3$] G-tetraplex. *Structure* 1993;**1**:263–82. https://doi.org/10.1016/0969-2126(93)90015-9
8. Parkinson GN, Lee MP, Neidle S. Crystal structure of parallel quadruplexes from human telomeric DNA. *Nature* 2002;**417**:876–80. https://doi.org/10.1038/nature755
9. Bryan TM. G-quadruplexes at telomeres: friend or foe? *Molecules* 2020;**25**:3686. https://doi.org/10.3390/molecules25163686
10. Vorlíčková M, Tomasko M, Sagi AJ *et al.* 8-Oxoguanine in a quadruplex of the human telomere DNA sequence. *FEBS J* 2012;**279**:29–39. https://doi.org/10.1111/j.1742-4658.2011.08396.x
11. Lech CJ, Lim JKC, Lim JMW *et al.* Effects of site-specific guanine C8-modifications on an intramolecular DNA G-quadruplex. *Biophys J* 2011;**101**:1987–98. https://doi.org/10.1016/j.bpj.2011.08.049
12. Bielskutė S, Plavec J, Podbevšek P. Impact of oxidative lesions on the human telomeric G-quadruplex. *J Am Chem Soc* 2019;**141**:2594–603. https://doi.org/10.1021/jacs.8b12748
13. Minnick DT, Pavlov YI, Kunkel TA. The fidelity of the human leading and lagging strand DNA replication apparatus with 8-oxodeoxyguanosine triphosphate. *Nucleic Acids Res* 1994;**22**:5658–64. https://doi.org/10.1093/nar/22.25.5658
14. SantaLucia J Jr, Hicks D. The thermodynamics of DNA structural motifs. *Annu Rev Biophys Biomol Struct* 2004;**33**:415–40. https://doi.org/10.1146/annurev.biophys.32.110601.141800
15. Zuker M. Mfold web server for nucleic acid folding and hybridization prediction. *Nucleic Acids Res* 2003;**31**:3406–15. https://doi.org/10.1093/nar/gkg595
16. Markham NR, Zuker M. DINAMelt web server for nucleic acid melting prediction. *Nucleic Acids Res* 2005;**33**:W577–81. https://doi.org/10.1093/nar/gki591
17. Zadeh JN, Steenberg CD, Bois JS *et al.* NUPACK: analysis and design of nucleic acid systems. *J Comput Chem* 2011;**32**:170–3. https://doi.org/10.1002/jcc.21596
18. Huguet JM, Bizarro CV, Forns N *et al.* Single-molecule derivation of salt dependent base-pair free energies in DNA. *Proc Natl Acad Sci USA* 2010;**107**:15431–6. https://doi.org/10.1073/pnas.1001454107
19. Huguet JM, Ribezzi-Crivellari M, Bizarro CV *et al.* Derivation of nearest-neighbor DNA parameters in magnesium from single molecule experiments. *Nucleic Acids Res* 2017;**45**:12921–31. https://doi.org/10.1093/nar/gkx1161
20. Hopfinger MC, Kirkpatrick CC, Znosko BM. Predictions and analyses of RNA nearest neighbor parameters for modified nucleotides. *Nucleic Acids Res* 2020;**48**:8901–13. https://doi.org/10.1093/nar/gkaa654
21. Plum GE, Grollman AP, Johnson F *et al.* Influence of the oxidatively damaged adduct 8-oxodeoxyguanosine on the conformation, energetics, and thermodynamic stability of a DNA duplex. *Biochemistry* 1995;**34**:16148–60. https://doi.org/10.1021/bi00049a030
22. Schibel AEP, Fleming AM, Jin Q *et al.* Sequence-specific single-molecule analysis of 8-oxo-7,8-dihydroguanine lesions in DNA based on unzipping kinetics of complementary probes in ion channel recordings. *J Am Chem Soc* 2011;**133**:14778–84. https://doi.org/10.1021/ja205653v
23. Singh SK, Szulik MW, Ganguly M *et al.* Characterization of DNA with an 8-oxoguanine modification. *Nucleic Acids Res* 2011;**39**:6789–801. https://doi.org/10.1093/nar/gkr275
24. Lipscomb LA, Peek ME, Morningstar ML *et al.* X-ray structure of a DNA decamer containing 7,8-dihydro-8-oxoguanine. *Proc Natl Acad Sci USA* 1995;**92**:719–23. https://doi.org/10.1073/pnas.92.3.719
25. Oda Y, Uesugi S, Ikehara M *et al.* NMR studies of a DNA containing 8-hydroxydeoxyguanosine. *Nucleic Acids Res* 1991;**19**:1407–12. https://doi.org/10.1093/nar/19.7.1407
26. Ovcherenko SS, Shernyukov AV, Nasonov DM *et al.* Dynamics of 8-Oxoguanine in DNA: Decisive Effects of Base Pairing and Nucleotide Context. *J Am Chem Soc* 2023;**145**:5613–17. https://doi.org/10.1021/jacs.2c11230
27. McCauley MJ, Furman L, Dietrich CA *et al.* Quantifying the stability of oxidatively damaged DNA by single-molecule DNA stretching. *Nucleic Acids Res* 2018;**46**:4033–43. https://doi.org/10.1093/nar/gky148
28. Wang MD, Schnitzer MJ, Yin H *et al.* Force and velocity measured for single molecules of RNA polymerase. *Science* 1998;**282**:902–7. https://doi.org/10.1126/science.282.5390.902
29. Li X, Pei YF, Zhang YS *et al.* Single-molecule mechanical unfolding of AT-rich chromosomal fragile site DNA hairpins: resolving the thermodynamic and kinetic effects of a single G-T mismatch. *J Phys Chem B* 2020;**124**:9365–70. https://doi.org/10.1021/acs.jpcb.0c06954
30. Landuzzi F, Viader-Godoy X, Cleri F *et al.* Detection of single DNA mismatches by force spectroscopy in short DNA hairpins. *J Chem Phys* 2020;**152**:074204. https://doi.org/10.1063/1.5139284
31. Zhao XC, Dong HL, Li XL *et al.* 5-Methyl-cytosine stabilizes DNA but hinders DNA hybridization revealed by magnetic tweezers and simulations. *Nucleic Acids Res* 2022;**50**:12344–54. https://doi.org/10.1093/nar/gkac1122
32. An N, Fleming AM, White HS *et al.* Nanopore detection of 8-oxoguanine in the human telomere repeat sequence. *ACS Nano* 2015;**9**:4296–307. https://doi.org/10.1021/acsnano.5b00722
33. Lee HT, Bose A, Lee CY *et al.* Molecular mechanisms by which oxidative DNA damage promotes telomerase activity. *Nucleic Acids Res* 2017;**45**:11752–65. https://doi.org/10.1093/nar/gkx789
34. Ji J, Sharma A, Pokhrel P *et al.* Dynamic structures and fast transition kinetics of oxidized G-quadruplexes. *Small* 2024;**20**:e2400485. https://doi.org/10.1002/smll.202400485
35. Fleming AM, Burrows CJ. G-quadruplex folds of the human telomere sequence alter the site reactivity and reaction pathway of guanine oxidation compared to duplex DNA. *Chem Res Toxicol* 2013;**26**:593–607. https://doi.org/10.1021/tx400028y
36. Hatzakis E, Okamoto K, Yang D. Thermodynamic stability and folding kinetics of the major G-quadruplex and its loop isomers formed in the nuclease hypersensitive element in the human c-Myc promoter: effect of loops and flanking segments on the stability of parallel-stranded intramolecular G-quadruplexes. *Biochemistry* 2010;**49**:9152–60.
37. Bell GI. Models for the specific adhesion of cells to cells. *Science* 1978;**200**:618–27. https://doi.org/10.1126/science.347575
38. Evans E, Ritchie K. Dynamic strength of molecular adhesion bonds. *Biophys J* 1997;**72**:1541–55. https://doi.org/10.1016/S0006-3495(97)78802-7
39. You HJ, Guo SW, Le SM *et al.* Two-state folding energy determination based on transition points in nonequilibrium single-molecule experiments. *J Phys Chem Lett* 2018;**9**:811–6. https://doi.org/10.1021/acs.jpclett.7b03123
40. Cocco S, Yan J, Léger JF *et al.* Overstretching and force-driven strand separation of double-helix DNA. *Phys Rev E* 2004;**70**:011910https://doi.org/10.1103/PhysRevE.70.011910
41. You H, Zeng X, Xu Y *et al.* Dynamics and stability of polymorphic human telomeric G-quadruplex under tension. *Nucleic Acids Res* 2014;**42**:8789–95. https://doi.org/10.1093/nar/gku581
42. Peng H, Zhang Y, Luo Q *et al.* Unfolding rates of 1:1 and 2:1 complex of CX-5461 and c-*MYC* promoter G-quadruplexes

revealed by single-molecule force spectroscopy. *Biophys Rep* 2024;**10**:180–9. https://doi.org/10.52601/bpr.2024.240018
43. Pei YF, Liu YJ, Xie CY *et al.* Detecting the formation kinetics of doxorubicin–DNA interstrand cross-link at the single-molecule level and clinically relevant concentrations of doxorubicin. *Anal Chem* 2020;**92**:4504–11. https://doi.org/10.1021/acs.analchem.9b05657
44. Zhang Y, Cheng Y, Luo Q *et al.* Distinguishing G-quadruplexes stabilizer and chaperone for *c-MYC* promoter G-quadruplexes through single-molecule manipulation. *J Am Chem Soc* 2024;**146**:3689–99. https://doi.org/10.1021/jacs.3c09074
45. Wang KB, Liu YS, Li YP *et al.* Oxidative damage induces a vacancy G-quadruplex that binds guanine metabolites: solution structure of a cGMP fill-in vacancy G-quadruplex in the oxidized gene promoter. *J Am Chem Soc* 2022;**144**:6361–72. https://doi.org/10.1021/jacs.2c00435
46. David SS, O'Shea VL, Kundu S. Base-excision repair of oxidative DNA damage. *Nature* 2007;**447**:941–50. https://doi.org/10.1038/nature05978
47. Fleming AM, Burrows CJ. 8-Oxo-7,8-dihydroguanine, friend and foe: epigenetic-like regulator versus initiator of mutagenesis. *DNA Repair (Amst)* 2017;**56**:75–83. https://doi.org/10.1016/j.dnarep.2017.06.009
48. Seeman NC, Sleiman HF. DNA nanotechnology. *Nat Rev Mater* 2017;**3**:17068. https://doi.org/10.1038/natrevmats.2017.68
49. Gros J, Rosu F, Amrane S *et al.* Guanines are a quartet's best friend: impact of base substitutions on the kinetics and stability of tetramolecular quadruplexes. *Nucleic Acids Res* 2007;**35**:3064–75. https://doi.org/10.1093/nar/gkm111
50. Gorini F, Ambrosio S, Lania L *et al.* The intertwined role of 8-oxodG and G4 in transcription regulation. *Int J Mol Sci* 2023;**24**:2031. https://doi.org/10.3390/ijms24032031

Received: January 8, 2025. **Revised:** May 11, 2025. **Editorial Decision:** May 26, 2025. **Accepted:** May 30, 2025
© The Author(s) 2025. Published by Oxford University Press on behalf of Nucleic Acids Research.
This is an Open Access article distributed under the terms of the Creative Commons Attribution-NonCommercial License (https://creativecommons.org/licenses/by-nc/4.0/), which permits non-commercial re-use, distribution, and reproduction in any medium, provided the original work is properly cited. For commercial re-use, please contact reprints@oup.com for reprints and translation rights for reprints. All other permissions can be obtained through our RightsLink service via the Permissions link on the article page on our site—for further information please contact journals.permissions@oup.com.